



Bullo Hindebu Rikitu · O. D. Makinde · Lemi Guta Enyadene

Unsteady mixed convection of a radiating and reacting nanofluid with variable properties in a porous medium microchannel

Received: 20 April 2021 / Accepted: 13 September 2021 / Published online: 30 September 2021
© The Author(s), under exclusive licence to Springer-Verlag GmbH Germany, part of Springer Nature 2021

Abstract In this study we investigated unsteady mixed convection flow and heat transfer of radiating and reacting nanofluid with variable transport properties in a microchannel filed with a saturated porous medium by taking into account the convective boundary conditions. The Buongiorno's nanofluid flow model is used to study the effects of the Brownian motion and the thermophoresis. The governing highly nonlinear partial differential equations corresponding to the momentum, energy and concentration profiles have been formulated and solved numerically by utilizing the semi-discretization finite difference method. The effect of each governing thermophysical parameters on the microchannel hydrodynamic and thermal behaviors is discussed with the usage of graphs. The numerical results indicate that the velocity and temperature profiles show an increasing behavior with the variable viscosity parameter, Eckert number, thermal Grashof number, solutal Grashof number, Prandtl number and chemical reaction parameter, whereas the concentration profile increases with increasing values of variable thermal conductivity parameter, porous medium shape parameter, Forchheimer number, Brownian motion parameter, Schmidt number, Biot number and radiation parameter. Moreover, the result reveals that the skin friction coefficient increases with suction/injection Reynolds number, porous medium shape parameter, thermal Grashof number, Schmidt number and Brownian motion parameter but decreases with Eckert number, thermophoresis parameter, Biot number and radiation parameter. Both the heat transfer and the mass transfer rates at both sides of the microchannel walls are higher for large values of suction/injection Reynolds number, porous medium shape parameter and variable viscosity parameter, while both are lower for large values of Eckert number, variable thermal conductivity parameter and radiation parameter. Besides, Grashof number, Schmidt number and Biot number indicate an increasing effect on both the heat transfer and mass transfer rates at the cold wall of the microchannel. The numerical simulation also reveals that Brownian motion parameter and thermophoresis parameter show an opposite effect on both heat transfer and mass transfer rates at both sides of the microchannel walls.

Keywords Microchannel · Nanofluids · Thermal radiation · Chemical reaction · Suction/injection · Porous medium

Mathematics Subject Classification 76T20 · 76S05 · 76D05 · 76M20

B. H. Rikitu (✉) · L. G. Enyadene
Department of Applied Mathematics, Adama Science and Technology University, Adama, Ethiopia
E-mail: hindebubu@gmail.com

L. G. Enyadene
E-mail: senalemi2007@gmail.com

O. D. Makinde
Faculty of Military Science, Stellenbosch University, Private Bag X2, Saldanha 7395, South Africa
E-mail: makinded@gmail.com

List of symbols

| | |
|---------------|---|
| a | Microchannel width |
| σ^* | Stefan Boltzmann constant |
| D_b | Brownian diffusion coefficient |
| k^* | Rosseland mean absorption coefficient |
| D_T | Thermal diffusion coefficient |
| q_r | Thermal radiative heat flux |
| u | Axial nanofluid velocity |
| Ec | Eckert number |
| V | Constant wall suction/injection velocity |
| A | Dimensionless nanofluid pressure |
| g | Acceleration due to gravity |
| Re | Suction/injection Reynolds number |
| $\mu(T)$ | Temperature-dependent nanofluid dynamic viscosity |
| γ | Dimensionless variable viscosity parameter |
| μ_0 | Initial nanofluid dynamic viscosity |
| λ | Dimensionless variable thermal conductivity parameter |
| γ_1 | Viscosity variation parameter |
| Pr | Prandtl number |
| ρ | Density of nanofluid |
| Gt | Thermal Grashof number |
| C | Nanoparticles concentration |
| Gt | Solutal Grashof number |
| C_p | Specific heat at constant pressure |
| S | Porous medium shape parameter |
| K | Permeability parameter |
| F | Forchheimer number |
| $k(T)$ | Temperature-dependent thermal conductivity of nanofluid |
| Nb | Brownian motion parameter |
| k_0 | Initial nanofluid thermal conductivity |
| Nt | Thermophoresis parameter |
| γ_2 | Thermal conductivity variation parameter |
| R | Radiation parameter |
| h_f | Convective heat transfer coefficient |
| α | Chemical reaction parameter |
| Γ | Heat capacity ratio |
| Sc | Schmidt number |
| T_0 | Initial temperature |
| Bi | Biot number |
| T_w | Right wall temperature |
| C_f | Coefficient of skin friction |
| T_f | Nanofluid temperature heating microchannel surface |
| Nu | Nusselt number/heat transfer rate |
| T | Temperature of nanofluid |
| η | Dimensionless microchannel width |
| P | Pressure of nanofluid |
| W | Dimensionless axial nanofluid velocity |
| t | Time |
| τ | Dimensionless time |
| b | Porous inertial resistance coefficient |
| θ | Dimensionless nanofluid temperature |
| Da | Darcy number |
| ϕ | Dimensionless nanoparticles concentration |
| ε | Rate of reaction |
| Sh | Sherwood number/mass transfer rate |

1 Introduction

Nowadays, the convective flows and heat transfer characteristics in microchannels are attracting important research interests due to the wide range of industrial and engineering applications including electronic cooling, cooling of computer chips, automotive heat exchangers, laser equipment, aerospace technology, heat sinks of MEMS-based devices, environmental control, pharmaceutical and biotechnological applications such as drug delivery and DNA sequencing [1–3]. Consequently, a number of research studies have been communicated comprising the analysis of fluid flow and heat transfer phenomena in microchannels. To mention few, Reddy et al. [4] investigated the combined effects of wall slip, viscous dissipation and Joule heating on MHD electro-osmotic peristaltic motion of Casson fluid through a rotating asymmetric microchannel. Meanwhile, the explanation of the influence of slim obstacle geometry on the flow and heat transfer in microchannels is given by Kmiotek and Kucab-Pietal [5]. Moreover, similar studies can be found in the literature [6–8].

Even though microchannels possess large heat transfer coefficients, a challenging limitation of microchannels is that these higher convection heat transfer coefficients come at the cost of greater pressure drop per unit length and hence greater requirement of pumping power in the microchannels flow geometries [9]. Besides, common heat transfer fluids or base fluids such as water, oils and ethylene are poor in heat transfer capabilities due to their low thermal conductivity. Because of the aforementioned reasons, novel technologies with the potential of improving the fluid transport properties such as thermal conductivity of the working fluid are of great interest for flows in microchannels once again. From this perspective, utilization of nanofluids is among the convection heat transfer augmentation techniques. The term nanofluid was first pioneered by Choi [10] in 1995 to indicate that nanofluids are engineered suspension or dispersion of nanometer-sized particles (1–100 nm) into the common base fluids. Nanofluids have higher thermal conductivity, better absorption capacity and wonderful stability.

The flow of nanofluids in microchannels has large-scale utilization particularly as coolants in industrial and technological processes such as electronics cooling, transportation (engine cooling/vehicle thermal management), space and nuclear system cooling, defense applications (cooling military devices and systems), cooling in chillers and refrigerators, cancer therapy, air conditioning, CPU, MEMS, drug delivery applications [11, 12]. Consequently, there are many researchers for instance [13–18] who are currently reporting their research works in line with flow and heat transfer phenomena of nanofluids in microchannels.

Further augmentation of heat transfer rates in microchannels as well as in heat exchangers can be achieved by the syndication of nanofluids with porous media. Porous medium is a solid matrix which is characterized by the presence of void spaces called pores which are interconnected by a network of channels where a fluid can move. Fluid flow and heat transfer in channels filled with porous media occur in a numerous areas of applications including storage of radioactive nuclear waste, transpiration cooling, filtration, geothermal extraction, crude oil extraction, heating and cooling in buildings, systems, underground water movement, biomedical sciences and so on [19–21]. Therefore, during the last decades the study of nanofluid flow in microchannels filled with porous media has been receiving prodigious interests by many researchers including [22–25].

Moreover, convective flows with simultaneous heat and mass transfer under the influence of thermal radiation field and chemical reaction arise in many branches of science and engineering applications such as chemical industry, drying and dehydration operations in chemical food processing plants, oxidation of solid materials, manufacturing of ceramics/glassware, petroleum industries, in space technology, solar power technology, electrical power generation, nuclear power plants and various propulsion devices for aircraft, missiles, satellites and cooling towers [26–28]. Such studies are presented by several authors [29–33].

The related literature reviewed above can establish that the analysis of nanofluid flow and heat transfer phenomena in microchannels has been presented. However, many of such studies were modeled through a single-phase flow model by neglecting the slip velocity between the particle and base fluid. Therefore, more investigations of nanofluids as a two-phase flow which is also known as the Buongiorno model [34] should be considered because the slip velocity between the particle and base fluid plays important role on the heat transfer performance of nanofluids particularly from the industrial applications point of view. There are few research articles in which the Buongiorno model was utilized to study nanofluids flow and heat transfer in microchannels filled with porous media. For instance, Rundora and Makinde [35] investigated buoyancy effects on unsteady reactive variable properties fluid flow in a channel filled with a porous medium. Similarly, very recently the analysis of unsteady mixed convection flow of variable viscosity nanofluid in a microchannel filled with a porous medium is presented by [36].

Microchannel flow usually exhibits high frictional resistance which causes high-temperature generation within the coolant fluid as a consequence of which thermal conductivity and dynamic viscosity of the fluid are

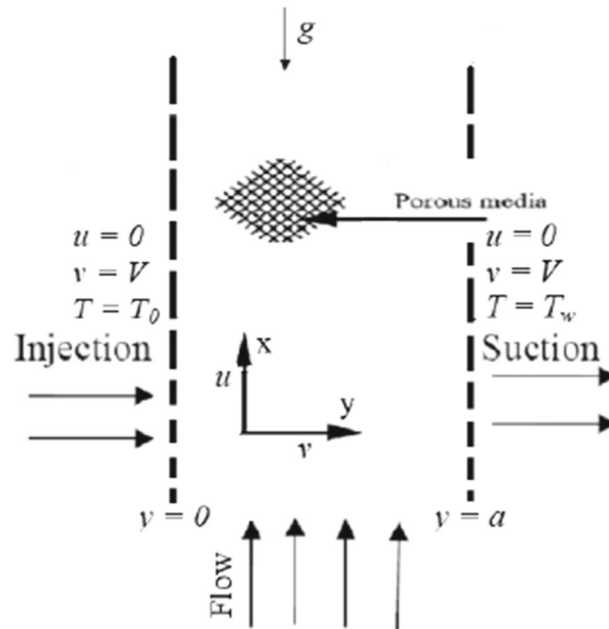


Fig. 1 Physical flow model with coordinate system

more likely to depend on temperature. Therefore, the above literature review is the motivation behind the main emphasis of this paper which is to examine the influence of porous material, convective boundary conditions, heat radiation and chemical reaction on unsteady mixed convection flow of nanofluid with variable transport properties past a permeable microchannel. Indeed, the work in the present paper is an extension of the work in [36]. The nonlinear function of thermal radiation is linearized with the use of Taylor series expansion, and the numerical solutions of modeled partial differential equations were obtained by means of semi-discretization finite difference method. Moreover, the influences of various pertinent parameters on the velocity, temperature, nanoparticles concentration, coefficient of skin friction, Nusselt number and Sherwood number are illustrated through graphs.

2 Mathematical model formulation

We consider unsteady mixed convective flow of Newtonian incompressible nanofluid in a microchannel filled with a saturated porous medium having permeable walls placed at $y = 0$ and $y = a$ as shown in Fig. 1, where a denotes the distance between two permeable walls of the microchannel.

It is assumed that the flow is driven by the combined actions of axial pressure gradient together with fluid body forces due to solutal and thermal buoyancy variations. Furthermore, a nanofluid injection into the microchannel takes place through the left wall ($y = 0$), while a nanofluid suction out of the microchannel occurs at the right wall ($y = a$). At time $t = 0$, the fluid temperature is maintained at T_0 and the fluid is in the static position. For large time ($t > 0$), the flow occurs only when the nanofluid starts to move with the time within the microchannel flow regime and is subjective to a convective heat exchange with the surrounding boundaries.

We also impose no-slip conditions for axial velocity at the walls, and the wall temperature is taken to be non-uniform where the left micro-channel wall is placed at temperature T_0 , while the right wall is placed at temperature T_w such that $T_0 < T_w$. Both the temperature and concentration are initially zero within the fluid except at the walls where the constant values are maintained.

The nanofluid dynamic viscosity is assumed to be an exponential decreasing function of temperature and hence given as $\mu(T) = \mu_0 e^{-\gamma_1(T-T_w)}$ where γ_1 is a viscosity variation parameter and μ_0 is the initial nanofluid dynamic viscosity at temperature T_0 . Besides, the thermal conductivity of the nanofluid is also assumed to be an exponential increasing function of temperature and hence given as $k(T) = k_0 e^{\gamma_2(T-T_w)}$ where γ_2 is the thermal conductivity variation parameter and k_0 is the initial nanofluid thermal conductivity at temperature T_0 . The axial convection terms are also assumed to be very small in the model equations and are neglected

as compared to the normal convection terms and thus $\frac{\partial T}{\partial x} \ll \frac{\partial T}{\partial y}$, $\frac{\partial C}{\partial x} \ll \frac{\partial C}{\partial y}$, $\frac{\partial u}{\partial x} \ll \frac{\partial u}{\partial y}$. Therefore, by considering the above assumptions and using the Darcy–Forchheimer flow model, the governing equations of continuity, linear momentum, energy and concentration under the usual Oberbeck–Boussinesq approximation are presented in the following form.

$$\frac{\partial u}{\partial x} = 0 \quad (1)$$

$$\frac{\partial u}{\partial t} + V \frac{\partial u}{\partial y} = -\frac{1}{\rho} \frac{\partial P}{\partial x} + \frac{1}{\rho} \frac{\partial}{\partial y} \left[\mu(T) \frac{\partial u}{\partial y} \right] - \frac{\mu(T)u}{\rho K} - \frac{bu^2}{\sqrt{K}} + \beta_1 g(T - T_w) + \beta_2 g(C - C_0) \quad (2)$$

$$\begin{aligned} \frac{\partial T}{\partial t} + V \frac{\partial T}{\partial y} = & \frac{1}{\rho C_p} \frac{\partial}{\partial y} \left[k(T) \frac{\partial T}{\partial y} \right] + \Gamma \left[D_B \frac{\partial C}{\partial y} \frac{\partial T}{\partial y} + \frac{D_T}{T_w} \left(\frac{\partial T}{\partial y} \right)^2 \right] + \frac{\mu(T)}{\rho C_p} \left(\frac{\partial u}{\partial y} \right)^2 + \frac{\mu(T)u^2}{\rho C_p K} \\ & + \frac{bu^3}{C_p \sqrt{K}} - \frac{1}{\rho C_p} \frac{\partial q_r}{\partial y} \end{aligned} \quad (3)$$

$$\frac{\partial C}{\partial t} + V \frac{\partial C}{\partial y} = D_B \frac{\partial^2 C}{\partial y^2} + \frac{D_T}{T_w} \frac{\partial^2 T}{\partial y^2} - \varepsilon(C - C_0) \quad (4)$$

With the initial and boundary conditions:

$$u(0, t) = 0, -k_0 \frac{\partial T}{\partial y}(0, t) = h_f(T_f - T(0, t)), \left. \begin{aligned} u(y, 0) = 0, T(y, 0) = T_w, C(y, 0) = C_0 \text{ and} \\ D_B \frac{\partial C(0, t)}{\partial y} = \frac{-D_T}{T_w} \frac{\partial T(0, t)}{\partial y}, \\ u(a, t) = 0, T(a, t) = T_w, \\ C(a, t) = C_1 \end{aligned} \right\} \text{for } t > 0 \quad (5)$$

where u is the axial velocity, V is constant wall suction/injection velocity, ρ is the nanofluid density, P is nanofluid pressure, T is the nanofluid temperature, C is the nanoparticles concentration, C_p is specific heat at constant pressure, Γ is the heat capacity ratio which is the ratio of heat capacity of the nanoparticle and heat capacity of base fluid, K is the porous medium permeability, g is gravitational acceleration, D_B is the Brownian diffusion coefficient, D_T is thermal diffusion coefficient, h_f is convective heat transfer coefficient, T_f is the temperature of the nanofluid heating the surface of the microchannel, ε is the reaction rate, q_r is the thermal radiative heat flux vector, and b is the second-order dimensionless (porous inertia) resistance coefficient also known as the dimensionless Forchheimer constant such that $b = 0$ corresponds to the Darcy law.

Radiation is a process which involves energy transfer by electromagnetic wave propagation which can occur in vacuum as well as in a medium. Experimental evidence indicates that radiant heat transfer is proportional to the fourth power of the absolute temperature, whereas conduction and convection are proportional to a linear temperature difference. From the Rosseland approximation, the radiative heat flux q_r in energy equation (3) is given by

$$q_r = -\frac{4\sigma^*}{3k^*} \frac{\partial T^4}{\partial y} \quad (6)$$

where σ^* and k^* represent the Stefan Boltzmann constant and the Rosseland mean absorption coefficient, respectively. The temperature difference within the flow is also assumed to be sufficiently small so that T^4 in Eq. (6) can be easily linearized about T_0 by using the Taylor series expansion as $T^4 = T_0^4 + 4T_0^3(T - T_0) + 6T_0^2(T - T_0)^2 + \dots$. Then neglecting the second- and higher-order terms, we have $T^4 \approx 4T_0^3T - 3T_0^4$. So, $\frac{\partial T^4}{\partial y} = 4T_0^3 \frac{\partial T}{\partial y}$. Now using this in Eq. (6) we get $q_r = -\frac{16\sigma^*T_0^3}{3k^*} \frac{\partial T}{\partial y}$. Therefore,

$$\frac{\partial q_r}{\partial y} = -\frac{16\sigma^*T_0^3}{3k^*} \frac{\partial^2 T}{\partial y^2} \quad (7)$$

Substituting Eq. (7) into energy equation (3) yields

$$\begin{aligned} \frac{\partial T}{\partial t} + V \frac{\partial T}{\partial y} = & \frac{1}{\rho C_p} \frac{\partial}{\partial y} \left[k(T) \frac{\partial T}{\partial y} \right] + \Gamma \left[D_B \frac{\partial C}{\partial y} \frac{\partial T}{\partial y} + \frac{D_T}{T_w} \left(\frac{\partial T}{\partial y} \right)^2 \right] + \frac{\mu(T)}{\rho C_p} \left(\frac{\partial u}{\partial y} \right)^2 + \frac{\mu(T)u^2}{\rho C_p K} \\ & + \frac{bu^3}{C_p \sqrt{K}} + \frac{1}{\rho C_p} \frac{16\sigma^*T_0^3}{3k^*} \frac{\partial^2 T}{\partial y^2} \end{aligned} \quad (8)$$

3 Non-dimensional formulation

In order to non-dimensionalize governing Eqs. (1)–(5) and (8), we introduce the following dimensionless variables.

$$\begin{aligned}
 \eta &= \frac{y}{a}, X = \frac{x}{a}, W = \frac{\rho au}{\mu_0}, \tau = \frac{\mu_0 t}{\rho a^2}, \theta = \frac{T - T_w}{T_w - T_0}, \phi = \frac{C - C_0}{C_1 - C_0}, P^* = \frac{\rho a^2 P}{\mu_0^2}, A = -\frac{\partial P^*}{\partial X}, \\
 Re &= \frac{\rho Va}{\mu_0}, \gamma = \gamma_1(T_w - T_0), \lambda = \gamma_2(T_w - T_0), S = \frac{a^2}{K}, F = \frac{ba}{\rho\sqrt{K}}, Bi = \frac{ah_f}{k_0}, \alpha = \frac{\varepsilon\rho a^2}{\mu_0}, \\
 Gt &= \frac{\beta_1 g \rho^2 a^3 (T_w - T_0)}{\mu_0^2}, Gc = \frac{\beta_2 g \rho^2 a^3 (C_1 - C_0)}{\mu_0^2}, Nt = \Gamma \frac{D_T}{T_w} (T_w - T_0) \frac{\rho}{\mu_0}, R = \frac{16\sigma^* T_0^3}{3k^* k_0}, \\
 Nb &= \Gamma D_B (C_1 - C_0) \frac{\rho}{\mu_0}, Ec = \frac{\mu_0^2}{\rho^2 a^2 C_p (T_w - T_0)}, Pr = \frac{\mu_0 C_p}{k_0}, Sc = \frac{\mu_0}{\rho D_B}
 \end{aligned} \tag{9}$$

Using the dimensionless variables defined in (9) into Eqs. (1)–(5) and (8) yields the following dimensionless governing equations.

$$\frac{\partial W}{\partial X} = 0 \tag{10}$$

$$\frac{\partial W}{\partial \tau} + Re \frac{\partial W}{\partial \eta} = A + e^{-\gamma\theta} \left[\frac{\partial^2 W}{\partial \eta^2} - \gamma \frac{\partial \theta}{\partial \eta} \frac{\partial W}{\partial \eta} \right] - Se^{-\gamma\theta} W - FW^2 + Gt\theta + Gc\phi \tag{11}$$

$$\begin{aligned}
 \frac{\partial \theta}{\partial \tau} + Re \frac{\partial \theta}{\partial \eta} &= \frac{1}{Pr} \left[e^{\lambda\theta} + R \right] \frac{\partial^2 \theta}{\partial \eta^2} + Nb \frac{\partial \phi}{\partial \eta} \frac{\partial \theta}{\partial \eta} + \left[Nt + \frac{1}{Pr} \lambda e^{\lambda\theta} \right] \left(\frac{\partial \theta}{\partial \eta} \right)^2 \\
 &+ Ece^{-\gamma\theta} \left(\frac{\partial W}{\partial \eta} \right)^2 + SEce^{-\gamma\theta} W^2 + FEcW^3
 \end{aligned} \tag{12}$$

$$\frac{\partial \phi}{\partial \tau} + Re \frac{\partial \phi}{\partial \eta} = \frac{1}{Sc} \left[\frac{\partial^2 \phi}{\partial \eta^2} + \frac{Nt}{Nb} \frac{\partial^2 \theta}{\partial \eta^2} \right] - \alpha\phi \tag{13}$$

The corresponding dimensionless initial and boundary conditions are:

$$\left. \begin{aligned}
 W(0, \tau) = 0, \frac{\partial \phi(0, \tau)}{\partial \eta} = -Bi[1 - \theta(0, \tau)], \\
 W(\eta, 0) = 0, \theta(\eta, 0) = 0, \phi(\eta, 0) = 0 \text{ and } Nb \frac{\partial \phi(0, \tau)}{\partial \eta} + Nt \frac{\partial \theta(0, \tau)}{\partial \eta} = 0, \\
 W(1, \tau) = 0, \theta(1, \tau) = 1, \\
 \phi(1, \tau) = 1
 \end{aligned} \right\} \text{for } \tau > 0 \tag{14}$$

where τ is dimensionless time, Re is the suction/injection Reynolds number, Gt is the Grashof number due to thermal buoyancy effect, Gc is the Grashof number due to solutal buoyancy effect, Ec is the Eckert number, Pr is the Prandtl number, A is dimensionless axial pressure gradient parameter, γ is the dimensionless viscosity variation parameter, λ is the dimensionless thermal conductivity variation parameter, S is the porous media shape factor parameter, and F is the Forchheimer number also called the Forchheimer inertial resistance which is the second-order porous media resistance parameter, R is radiation parameter, Sc is the Schmidt number, Nb is the Brownian motion parameter, Nt is the thermophoresis parameter, α is dimensionless reaction rate parameter, and Bi is the Biot number for the microchannel.

Other physical quantities of practical significance in this study are the skin friction coefficient C_f , the local Nusselt number Nu and the local Sherwood number Sh , and thus, C_f , Nu , Sh at the microchannel walls take the following dimensionless form.

$$C_f = e^{-\gamma\theta} \left. \frac{dW}{d\eta} \right|_{\eta=0,1}, \quad Nu = -\left. \frac{d\theta}{d\eta} \right|_{\eta=0,1}, \quad Sh = -\left. \frac{d\phi}{d\eta} \right|_{\eta=0,1} \tag{15}$$

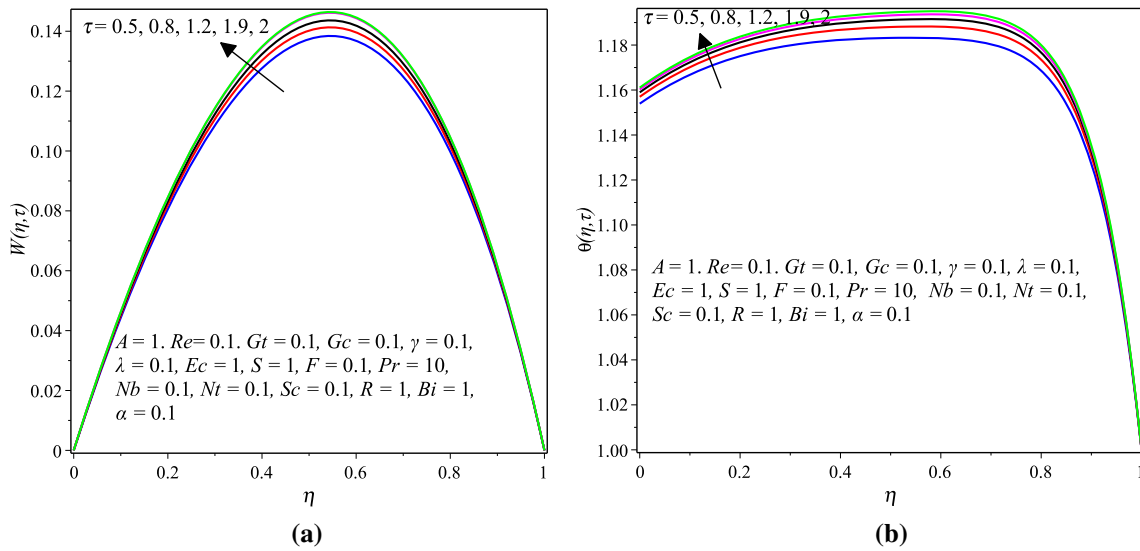


Fig. 2 a Velocity and b temperature profiles with transient and steady-state solutions

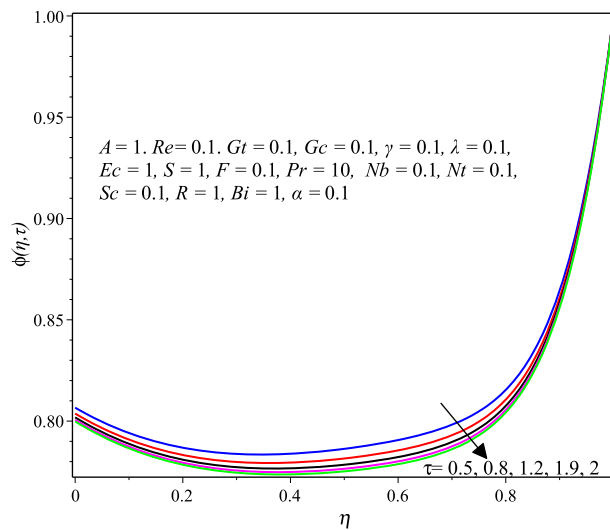


Fig. 3 Concentration profile with transient and steady-state solution

4 Method of numerical solution

The finite difference numerical method adopted to tackle obtained model initial boundary value problem (IBVP) (11)–(14) is the method of lines. The method is numerically stable with a high level of accuracy based on the well-known fourth-order Runge–Kutta integration scheme [37]. The numerical approach includes transforming the obtained IBVP into initial value problem (IVP) by discretizing centrally in space only. Thereafter, the obtained IVP is numerically solved using the fourth-order Runge–Kutta integration scheme. Thus, the semi-discretization scheme for the velocity, temperature and concentration fields is recorded as follows.

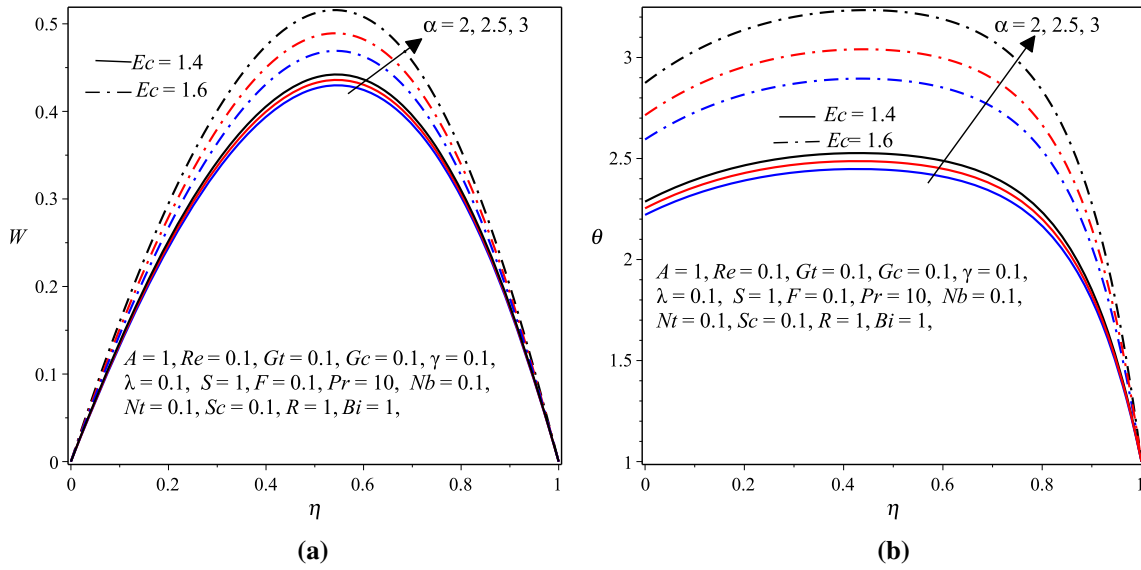


Fig. 4 **a** Velocity and **b** temperature profiles with varying Ec and α



Fig. 5 **a** Effects of Ec and α and **b** γ and λ on the concentration profile

$$\begin{aligned} \frac{dW_i}{d\tau} = & A - Re \frac{W_{i+1} - W_{i-1}}{2\Delta\eta} - e^{-\gamma\theta_i} S W_i - F W_i^2 + G t \theta_i + G c \phi_i \\ & + e^{-\gamma\theta_i} \left[\frac{W_{i-1} - 2W_i + W_{i+1}}{(\Delta\eta)^2} - \gamma \frac{\theta_{i+1} - \theta_{i-1}}{2\Delta\eta} \cdot \frac{W_{i+1} - W_{i-1}}{2\Delta\eta} \right] \end{aligned} \quad (16)$$

$$\begin{aligned} \frac{d\theta_i}{d\tau} = & -Re \frac{\theta_{i+1} - \theta_{i-1}}{2\Delta\eta} + \frac{1}{Pr} \left[e^{-\lambda\theta_i} + R \right] \left[\frac{\theta_{i-1} - 2\theta_i + \theta_{i+1}}{(\Delta\eta)^2} \right] + Nb \frac{\phi_{i+1} - \phi_{i-1}}{2\Delta\eta} \cdot \frac{\theta_{i+1} - \theta_{i-1}}{2\Delta\eta} \\ & + \left[Nt + \frac{1}{Pr} \lambda e^{\lambda\theta_i} \right] \left[\frac{\theta_{i+1} - \theta_{i-1}}{2\Delta\eta} \right]^2 + E c e^{-\gamma\theta_i} \left[\frac{W_{i+1} - W_{i-1}}{2\Delta\eta} \right]^2 + S E c e^{-\gamma\theta_i} W_i^2 + F E c W_i^3 \end{aligned} \quad (17)$$

$$\frac{d\phi_i}{d\tau} = -Re \frac{\phi_{i+1} - \phi_{i-1}}{2\Delta\eta} + \frac{1}{Sc} \left[\frac{\phi_{i-1} - 2\phi_i + \phi_{i+1}}{(\Delta\eta)^2} + \frac{Nt}{Nb} \cdot \frac{\theta_{i-1} - 2\theta_i + \theta_{i+1}}{(\Delta\eta)^2} \right] - \alpha \phi_i \quad (18)$$

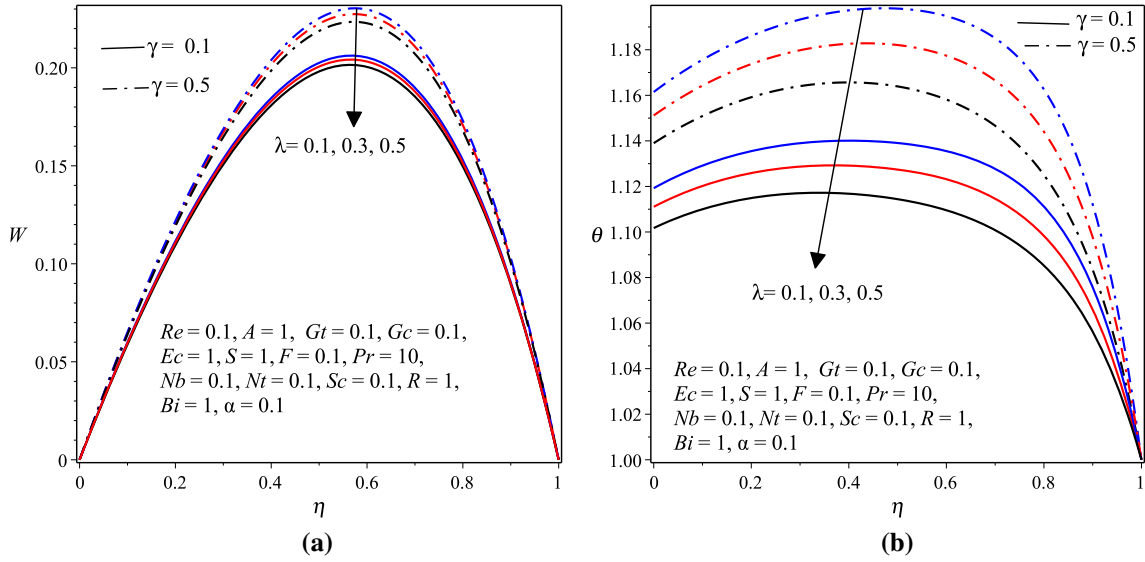


Fig. 6 **a** Velocity and **b** temperature profiles with varying γ and λ

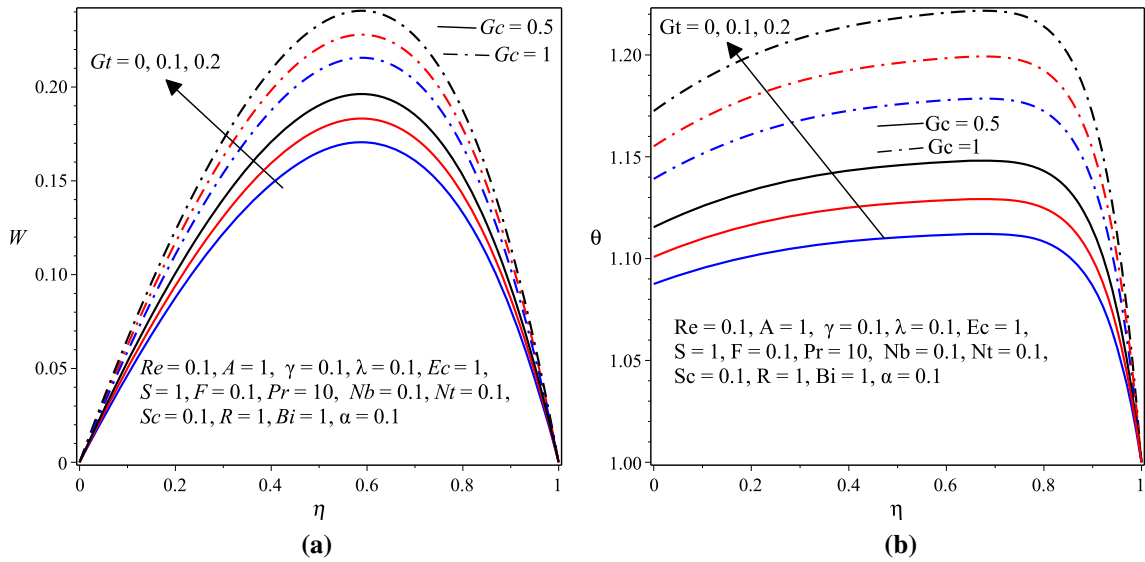


Fig. 7 **a** Velocity and **b** temperature profiles with varying Gt and Gc

The initial conditions are

$$W_i(0) = 0, \quad \theta_i(0) = 0, \quad \phi_i(0) = 0 \quad (19)$$

where $W_i(\tau) = W(\eta_i, \tau)$, $\theta_i(\tau) = \theta(\eta_i, \tau)$, $\phi_i(\tau) = \phi(\eta_i, \tau)$ and the spatial interval $[0, 1]$ partitioned into N equal sub-intervals. The grid size and the grid points are defined as $\Delta\eta = \frac{1}{N}$ and $\eta_i = \frac{i-1}{\Delta\eta}$ for $1 \leq i \leq N + 1$.

5 Results and discussion

This section presents the detailed overview of numerical outcomes and physical interpretation of the effects of various embedded parameters such as A , Re , Ec , Gt , Gc , S , F , γ , λ , Nt , Nb , Pr , Sc , α , Bi , R on the flow field variables (W , θ , ϕ) as well as on the physical quantities of engineering interests (C_f , Nu , Sh). Suitable ranges for these governing flow parameters are: $1 \leq A \leq 1.3$, $0.1 \leq Re \leq 1$, $0.1 \leq Ec \leq 1.6$, $0.1 \leq \gamma$, $\lambda \leq 0.5$, $0 \leq Gt \leq 0.2$, $0.1 \leq Gc \leq 1$, $0.1 \leq S$, $F \leq 3.5$, $0.001 \leq Nt \leq 0.1$, $0.1 \leq Nb \leq 0.25$,

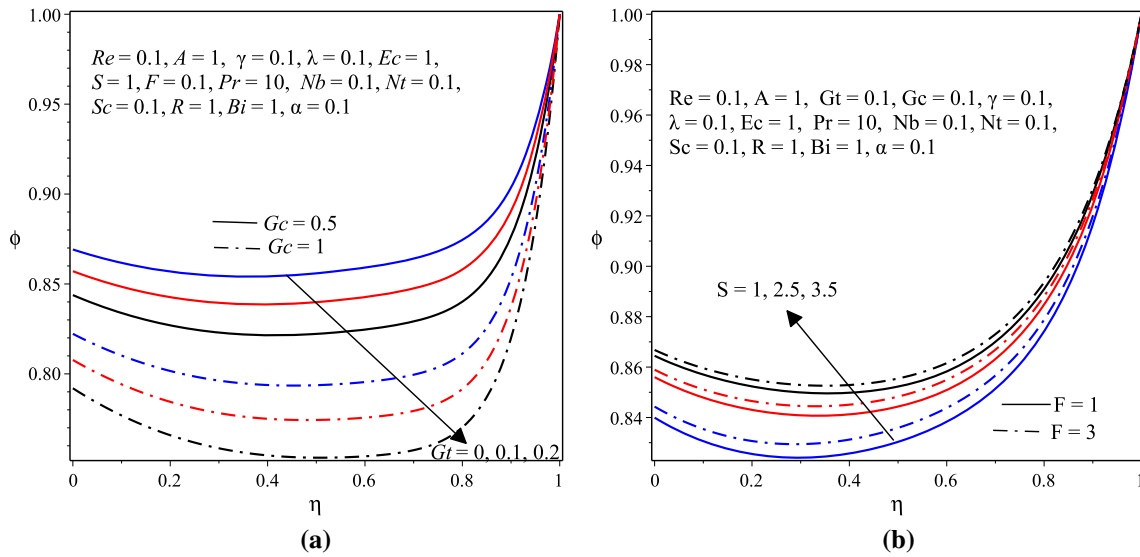


Fig. 8 a Effects of Gt and Gc and b effects of S and F on the concentration profile

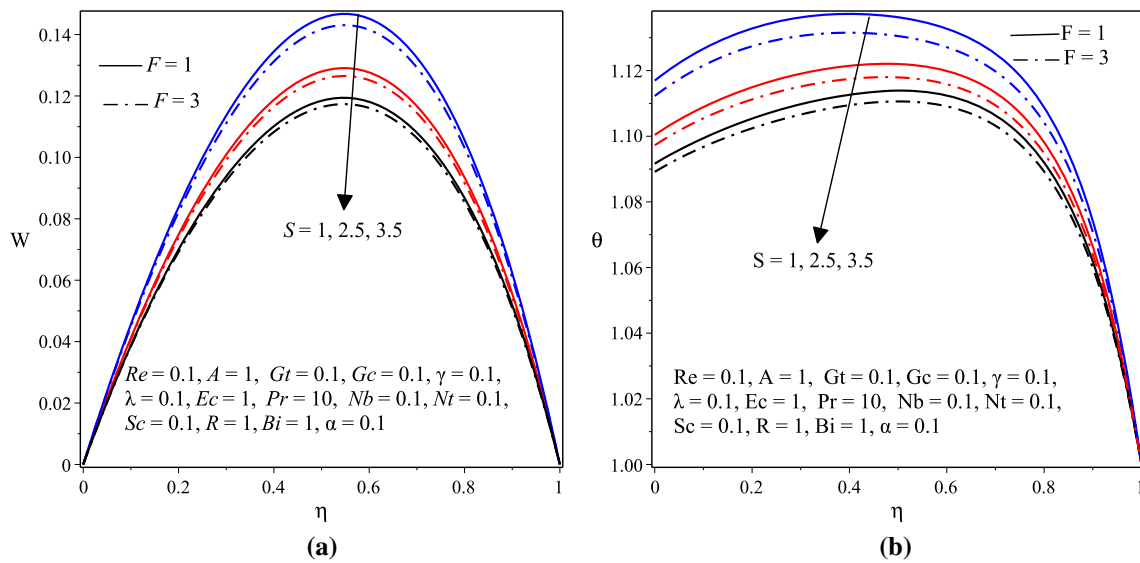


Fig. 9 a Velocity and b temperature profiles with varying S and F

$7 \leq Pr \leq 10$, $0.1 \leq Sc \leq 1.7$, $0.1 \leq \alpha \leq 3$, $1 \leq Bi \leq 2$, $0.3 \leq R \leq 1$. The reason of selecting such values for the parameters is to enable the effects of increasing or decreasing each of the embedded parameters on the radiating and reacting nanofluid flow structure and heat transfer enhancement capability in the microchannel. Moreover, for engineering and industrial applications, the regulation of the embedded parameters is necessary for optimal performance of the system.

5.1 Transient and steady-state profiles

The transient and steady-state profiles for the fluid velocity, temperature and concentration are portrayed in Figs. 2a, b and 3, respectively. From these figures it can be observed that the velocity, temperature and concentration profiles show a parabolic shape with transient increase and attain the steady states at about $\tau \geq 1.9$. In addition, Fig. 2a shows that the velocity profile attains its maximum value around the microchannel center line region and then reduces to zero because of the no-slip boundary conditions. Figure 2b demonstrates that the temperature profile attained its lowest value at the cold wall and gradually increasing toward the hot

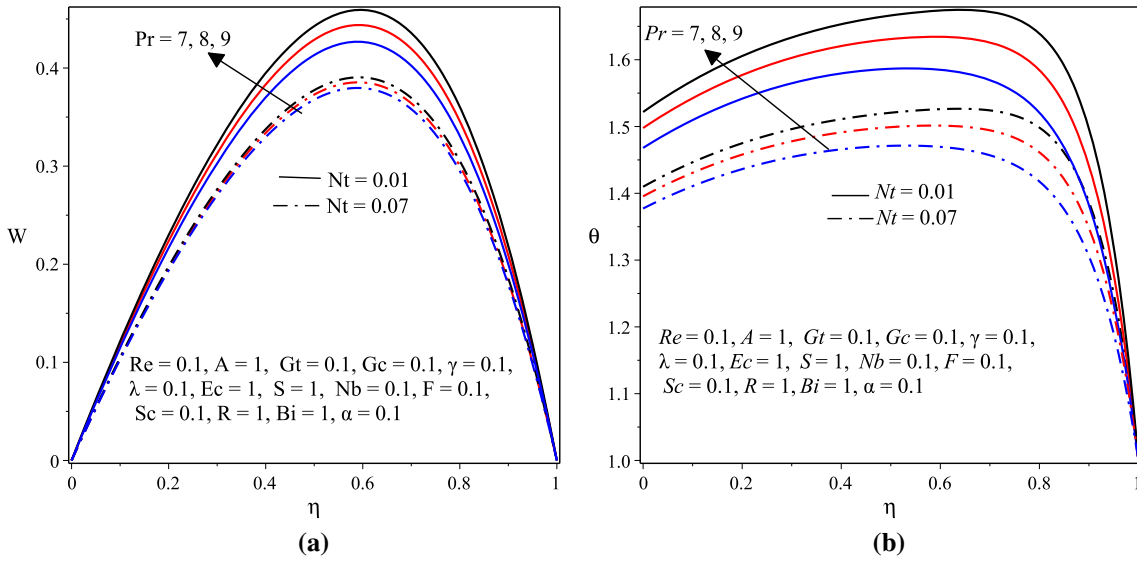


Fig. 10 **a** Velocity and **b** temperature profiles with varying Pr and Nt

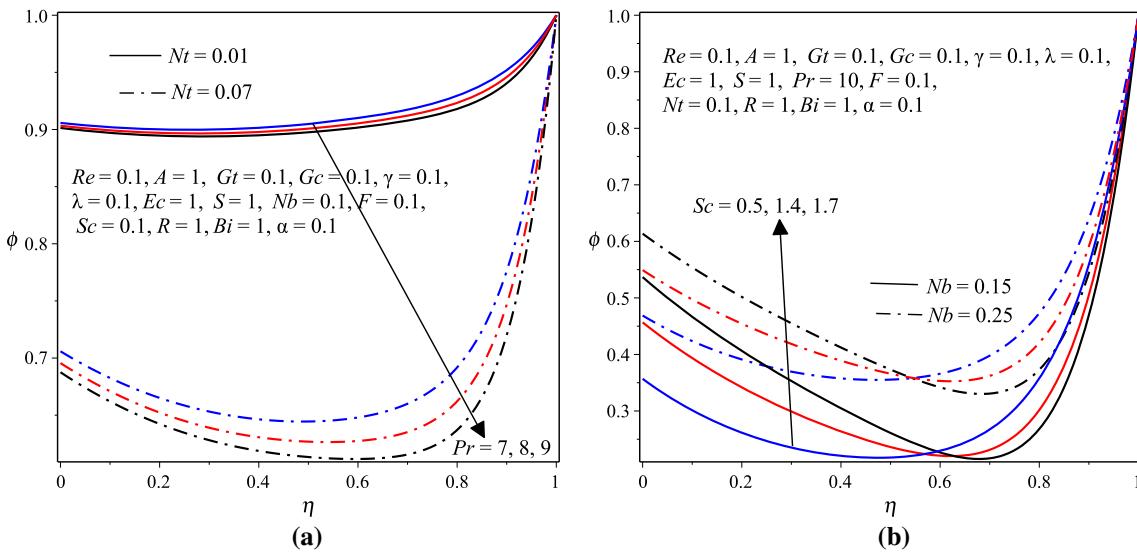


Fig. 11 **a** Effects of Pr and Nt and **b** effects of Sc and Nb on the concentration profile

wall where it attained its maximum value, whereas Fig. 3 indicates that the concentration profile attained its maximum value at the cold wall and starts declining gradually toward the hot wall where it attains its lowest value.

5.2 Parameter dependency of solutions

From Fig. 4a, b it is observed that as the magnitude of the Eckert number Ec increases, both the nanofuid velocity and temperature profiles increase. From the literature, the studies in [38,39] reported similar results. However, the concentration profile shows a retarding trend with increasing values of the Eckert number Ec as presented in Fig. 5a. This result is similar to the one obtained in [40]. Figure 4a, b also displays that both the nanofuid velocity and temperature profiles increase with the chemical reaction parameter α . References [40,41] reported similar findings. Unlike, from Fig. 5a it is observed that an increment in α shows a retarding effect on the concentration profile. This is because of the fact that the reactants are consumed during the homogeneous reaction and thus a decrease in the concentration is observed.

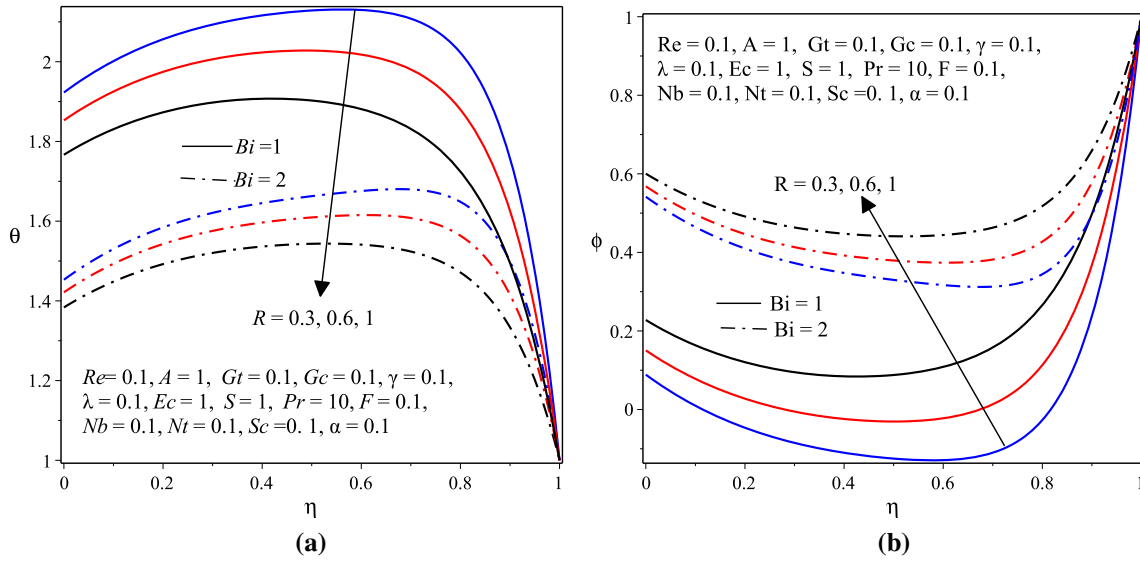


Fig. 12 a Temperature and b concentration profiles with varying Bi and R

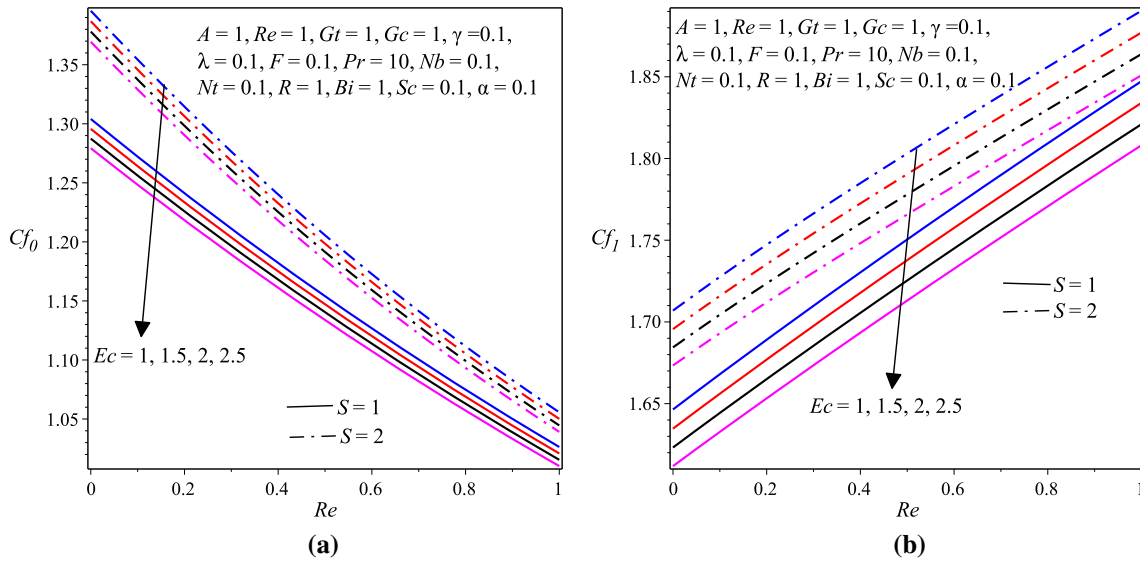


Fig. 13 a Cf at $\eta = 0$ and b Cf at $\eta = 1$ with varying S, Ec and Re

Figure 6a, b pictures that as the dimensionless variable viscosity parameter γ increases, a significant rise in the fluid velocity and temperature profiles is observed. This is the case because an increase in γ reduces the fluid viscosity since $\mu(T) = \mu_0 e^{-\gamma\theta}$. So, the fluid becomes less viscous and hence friction between fluid layers decreases due to which fluid velocity remains at higher levels for higher values of γ . The research works in [39,41] indicated similar results. However, increasing the values of the variable thermal conductivity parameter λ decreases the nanofluid velocity and temperature. A similar outcome was reported in [41]. Figure 5b shows the opposite trend for the concentration profile.

Figure 7a, b displays the effects of the thermal Grashof number Gt and the solutal Grashof number Gc on velocity and temperature profiles. The velocity and temperature profiles increase with Gt and Gc as shown in Fig. 7a, b. This is the case because as the values of Gt and Gc enhanced, the body forces acting on the fluid (thermal and solutal buoyancy forces) also get enhanced which also enhance the velocity that in turn increases the viscous heating, hence increasing the fluid temperature. The study in [39,40] revealed similar results. The opposite scenario is demonstrated in Fig. 8a for the concentration profile.

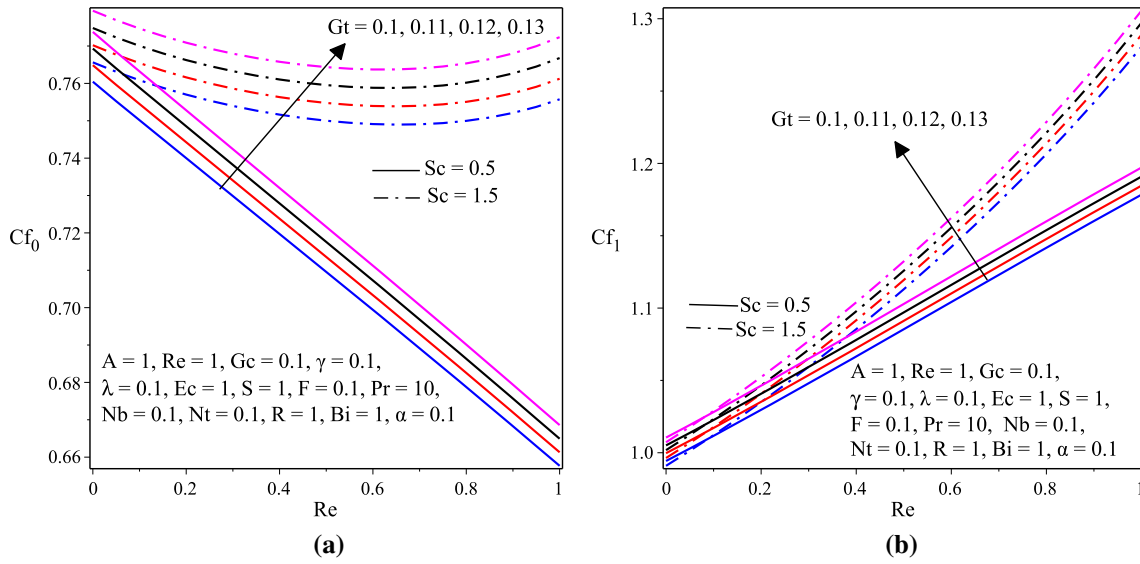


Fig. 14 a Cf at $\eta = 0$ and b Cf at $\eta = 1$ with varying Sc , Gt and Re

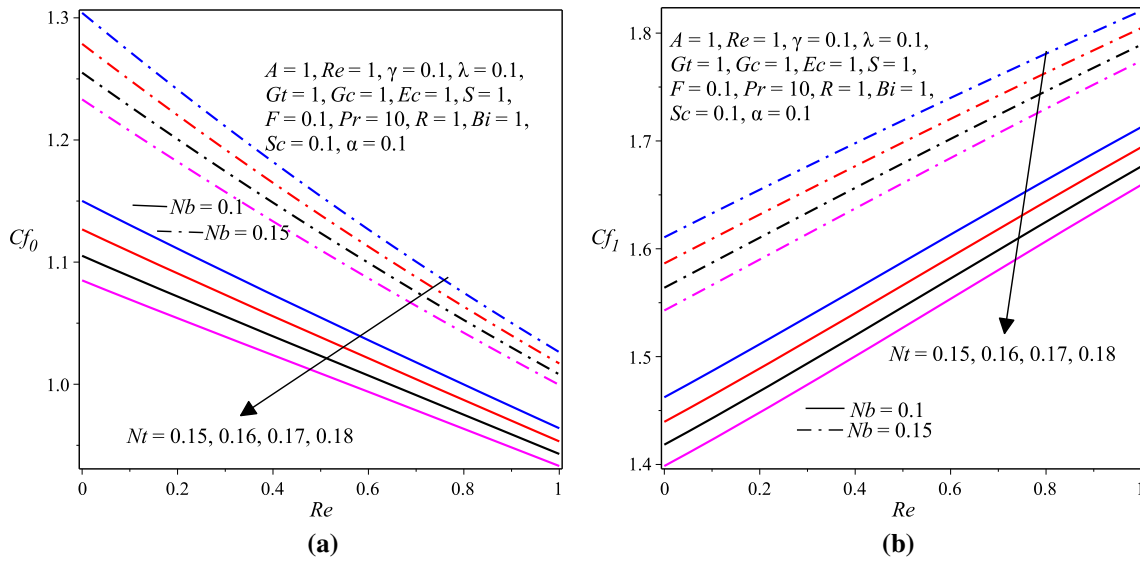


Fig. 15 a Cf at $\eta = 0$ and b Cf at $\eta = 1$ with varying Nt , Nb and Re

Figure 9a, b depicts the effects of the porous medium parameters S and F on the velocity and temperature profiles. Figure 9a, b portrays that both the velocity and temperature profiles decrease significantly as the porous medium shape parameter S increases. The reason behind this result is the fact that as the value of S increases, the porous medium permeability decreases which should naturally dampens the fluid flow and thus the observed decline in the magnitude of fluid velocity which also results in the decrement of viscous heating which in turn decreases the magnitude of fluid temperature. Besides, from the same figures it is observed that the fluid velocity and temperature profiles decrease with increasing values of the Forchheimer number F which is also known as inertial resistance parameter. Physically, large values of F imply the stronger resistant inertial force in the direction normal to the fluid flow which is due to the intensive dimensionless drag force coefficient b since $F = \frac{ba}{\rho\sqrt{K}}$. For higher values of b stronger resistivity inertial force is effective within the fluid flow so that the velocity becomes lessen and consequently the fluid temperature decreases. These results are similar to the findings in the works of [42]. On the contrary, Fig. 8b reveals that as both S and F increase, the concentration profile decreases.

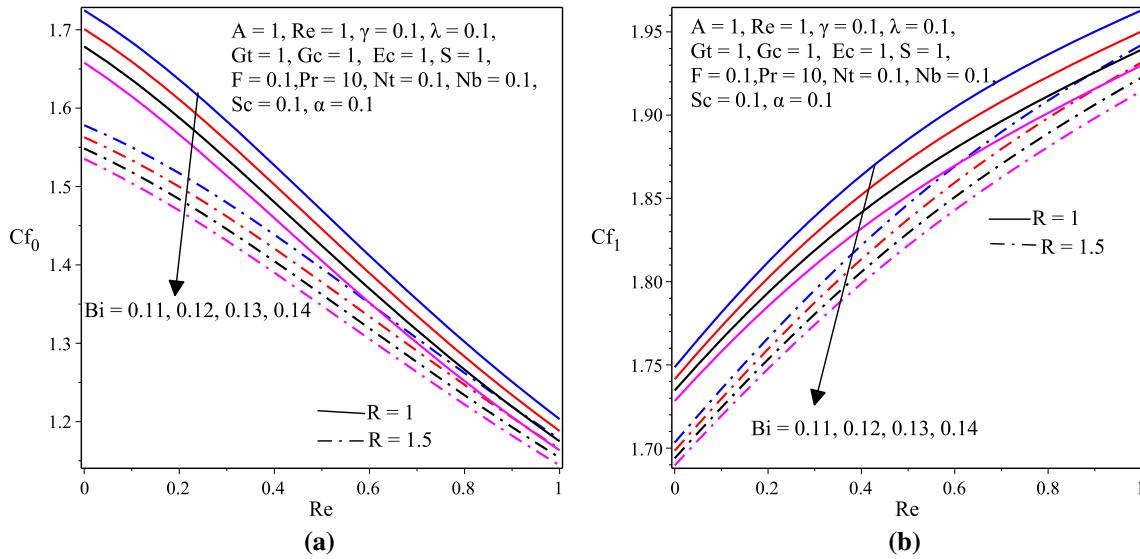


Fig. 16 a Cf at $\eta = 0$ and b Cf at $\eta = 1$ with varying Bi , R and Re

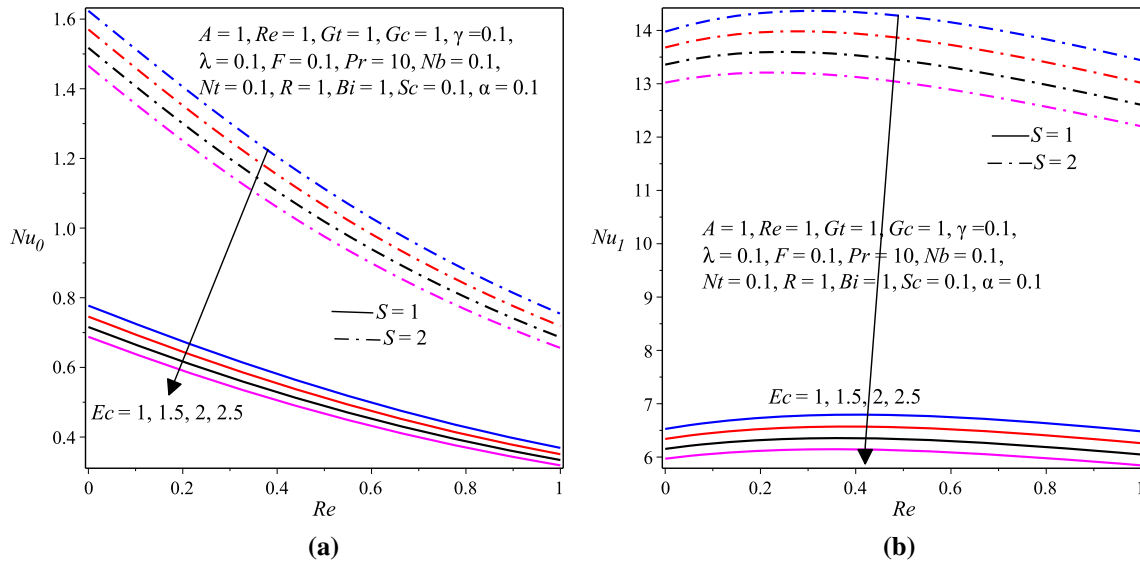


Fig. 17 a Nu at $\eta = 0$ and b Nu at $\eta = 1$ with varying Ec , S and Re

Figure 10a, b is double graphs that display the effects of the Prandtl number Pr and the thermophoresis parameter Nt on the velocity and temperature profiles. According to Fig. 10a the larger values of Pr lead to a significant increase in the velocity and temperature profiles since Pr is the ratio of momentum diffusivity to thermal diffusivity; therefore, the elevated values of Pr enhance the momentum diffusivity that results in enhancement of the velocity and temperature profiles. From the literature, [41,43] indicated similar findings. On the other hand, thermophoresis is a mechanism in which small particles are pulled away from hot region to cold one and thus Fig. 10a, b declares that as the value of Nt enhances, the velocity and temperature profiles decline. The reason behind this argument is that an enhancement in Nt yields a stronger thermophoretic force which allows deeper migration of nanoparticles from hot nanofluid to the cold surface resulting in lower fluid temperature. Figure 11a shows that the concentration profile decreases with both the Prandtl number Pr and the thermophoresis parameter Nt . Actually, these outcomes confirm the results reported in [40,41,43].

Figure 11b is also a double graph that portrays the effects of Sc and Nb on the concentration profile. This figure displays that the concentration profile increases with the Schmidt number Sc . Physically, larger values of Schmidt number Sc indicate less mass diffusion which causes the concentration of nanoparticles

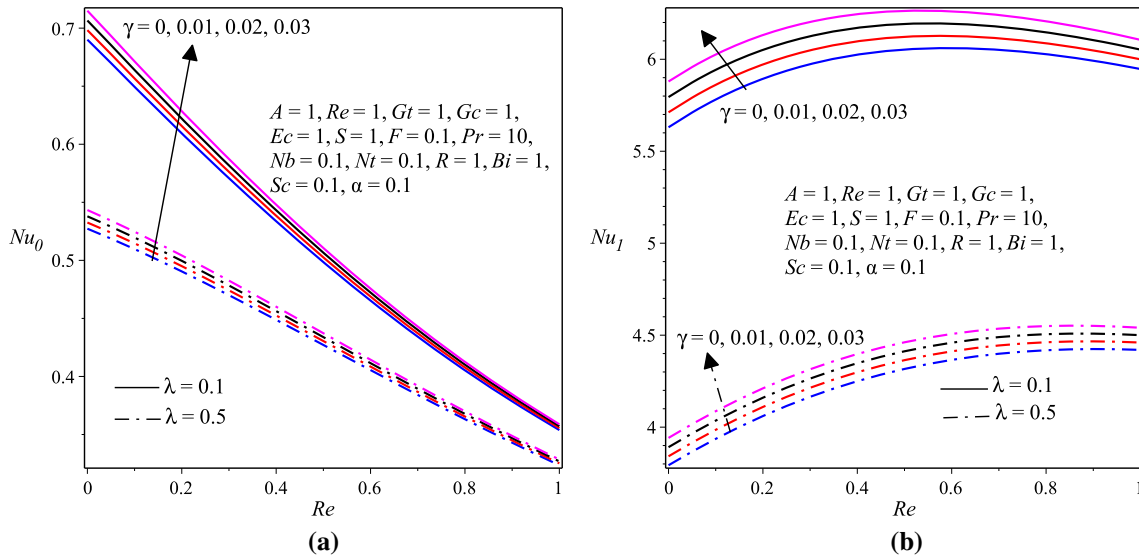


Fig. 18 a Nu at $\eta = 0$ and b Nu at $\eta = 1$ with varying γ , λ and Re

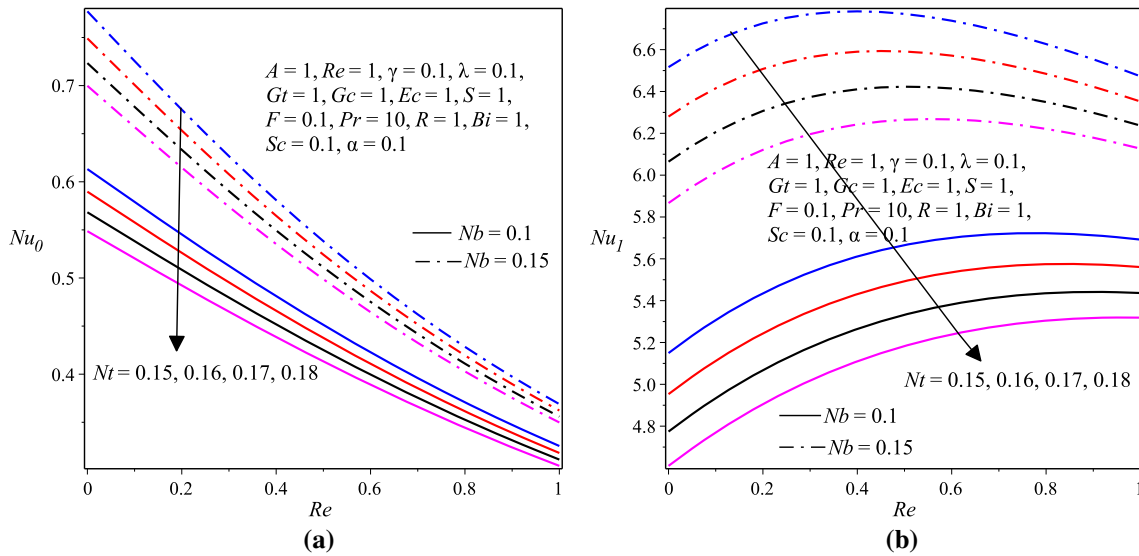


Fig. 19 a Nu at $\eta = 0$ and b Nu at $\eta = 1$ with varying Nt , Nb and Re

to remain larger in the fluid. The same results were obtained in the references [41,43,44]. The concentration profile also shows an increasing behavior for larger values of the Brownian motion parameter Nb as shown in Fig. 11b. The argument behind this result may be when the magnitudes of Nb increase, arbitrary disorganized motion and also collision of the nanoparticles in the fluid increase which may enhance the concentration of the nanoparticles in the fluid. The same result was presented by [40].

The effects of the radiation parameter R and the Biot number Bi on the nanofluid temperature and concentration profiles are displayed in Fig. 12a, b, respectively. Consequently, from Fig. 12a it is observed that the temperature profile decreases as R increases due to the fact that when a large value of radiative heat is absorbed by the nanofluid, the buoyancy force decreases which retards the flow rate, thereby retarding the temperature profiles. Thus, R quite effectively controls the microchannel temperature distribution and flow transport which plays a significant role in cooling the system. These types of applications can be used in pseudoscientific alternative medicine to control blood pressure through the process of magnetoelectric machine therapy. The results obtained in this paper are similar to the one obtained in [41,43,44]. From the same figure, it is also noticed that the temperature distribution declines with increased values of the Biot number Bi . This is the

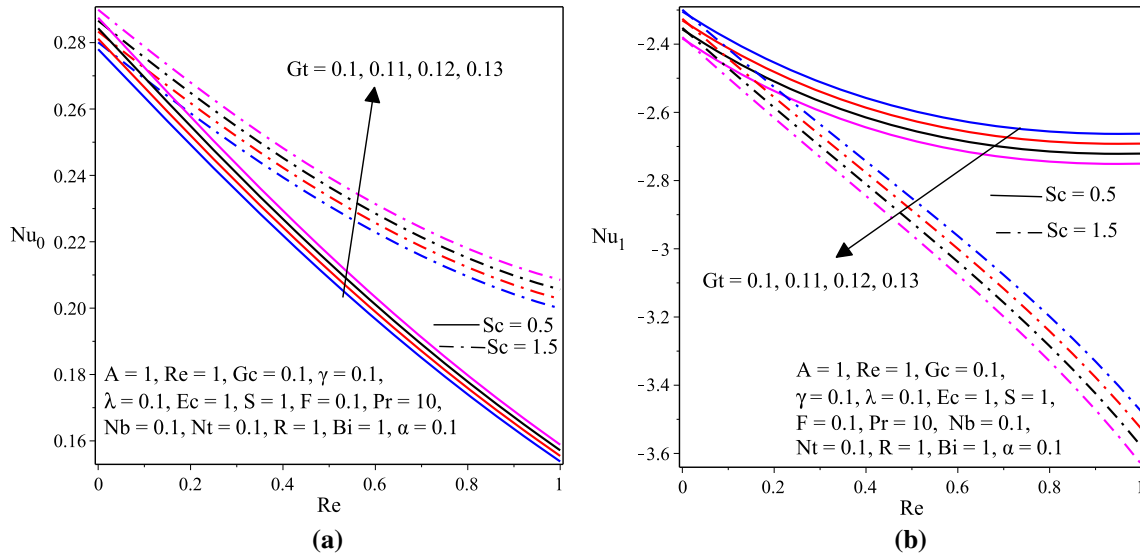


Fig. 20 a Nu at $\eta = 0$ and b Nu at $\eta = 1$ with varying Sc, Gt and Re

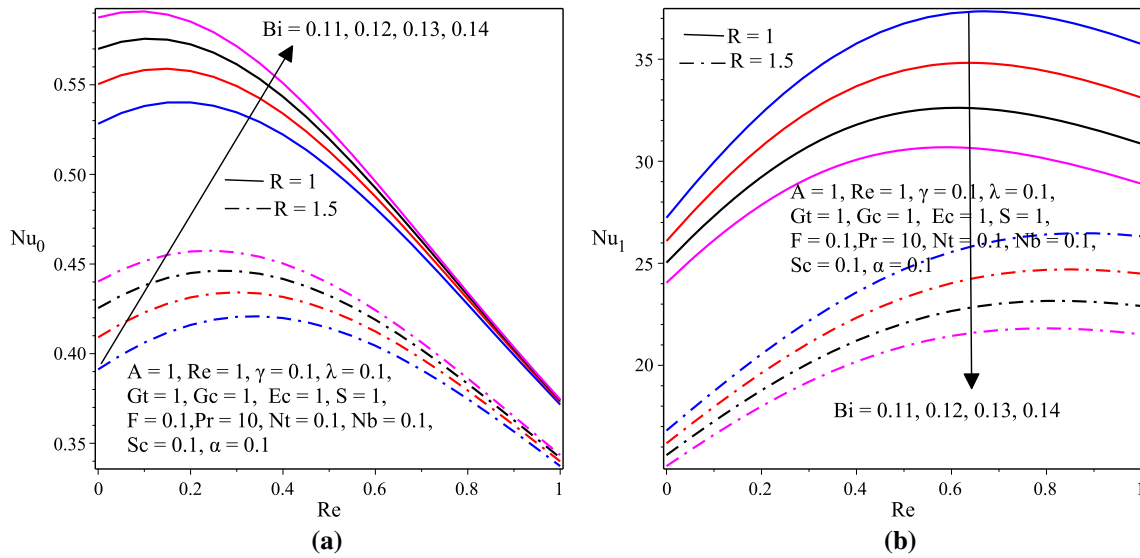


Fig. 21 a Nu at $\eta = 0$ and b Nu at $\eta = 1$ with varying Bi, R and Re

case because increment in Bi results in enhanced convective heat transport that results in the lowering of the temperature field. In the contrary, the radiation parameter R and the Biot number Bi indicate rising effects on the concentration profile as displayed in Fig. 12b. These results are the same as the result reported in the work of [39].

5.3 The wall shear stress, wall heat transfer and mass transfer rates

This subsection comprises the effects of flow parameters on the wall shear stress, wall heat and mass transfer rates. Indeed, the graphical results that are illustrated in this subsection for the skin friction coefficient C_f , the Nusselt number Nu and the Sherwood number Sh are plotted for large time, say $\tau \geq 1.9$ (steady state) and thus the results obtained may not be affected by time increasing for all parameters values as a consequence of the results obtained in Sect. 5.1.

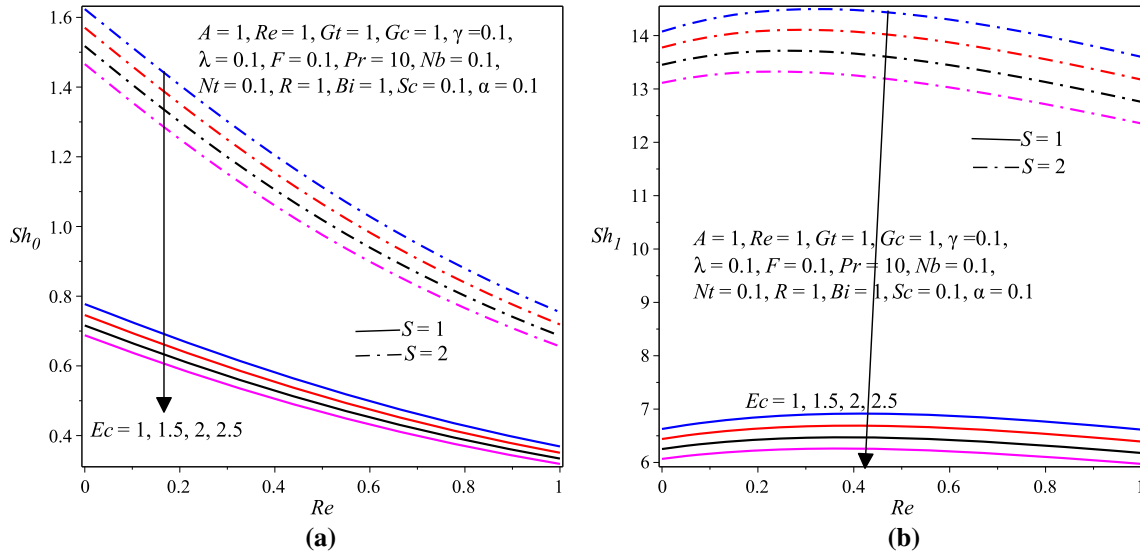


Fig. 22 a Sh at $\eta = 0$ and b Sh at $\eta = 1$ with varying Ec, S and Re

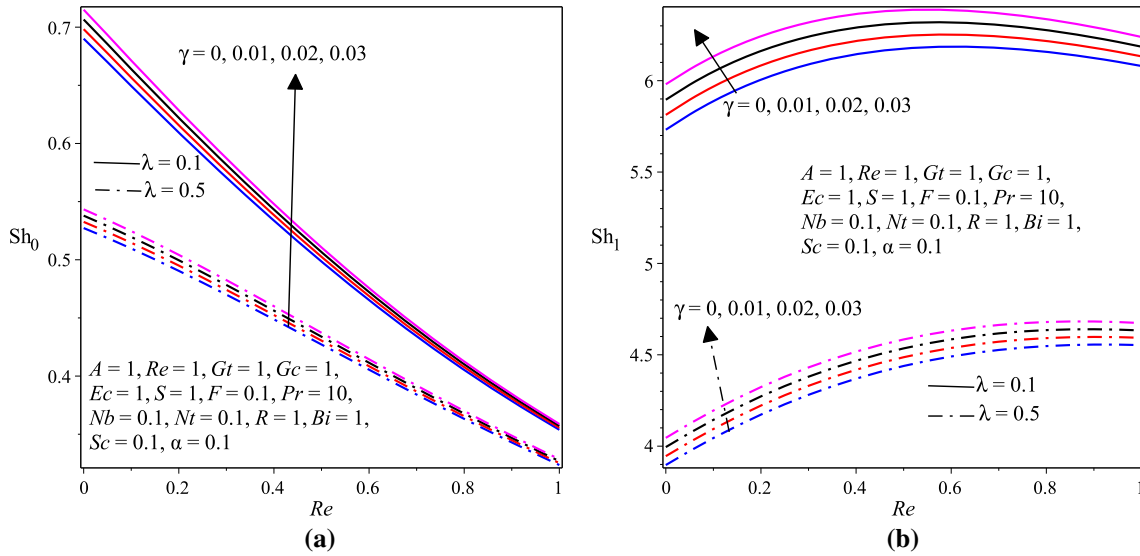


Fig. 23 a Sh at $\eta = 0$ and b Sh at $\eta = 1$ with varying γ, λ and Re

5.3.1 The wall shear stress: skin friction coefficient

The effects of pertinent parameters on the wall shear stress at the cold wall $\eta = 0$ and at the hot wall $\eta = 1$ are illustrated in Figs. 13a, 14, 15 and 16b. Consequently, from these graphs it is observed that the coefficient of skin friction C_f at both cold and hot walls shows an increasing behavior with increasing values of the thermal Grashof number Gt , the Schmidt number Sc , the Brownian motion parameter Nb and the porous medium shape parameter S for varying scaled values of the suction/injection Reynolds number Re . However, the Eckert number Ec , the thermophoresis parameter Nt , the radiation parameter R and the Biot number Bi indicate a decreasing effect on C_f at both walls of the microchannel.

5.3.2 The wall heat transfer rate: Nusselt number

The effects of pertinent governing flow parameters on the wall heat transfer rate at the cold wall $\eta = 0$ and at the hot wall $\eta = 1$ are portrayed in Figs. 17a, 18, 19, 20 and 21b. Consequently, from these graphs it can

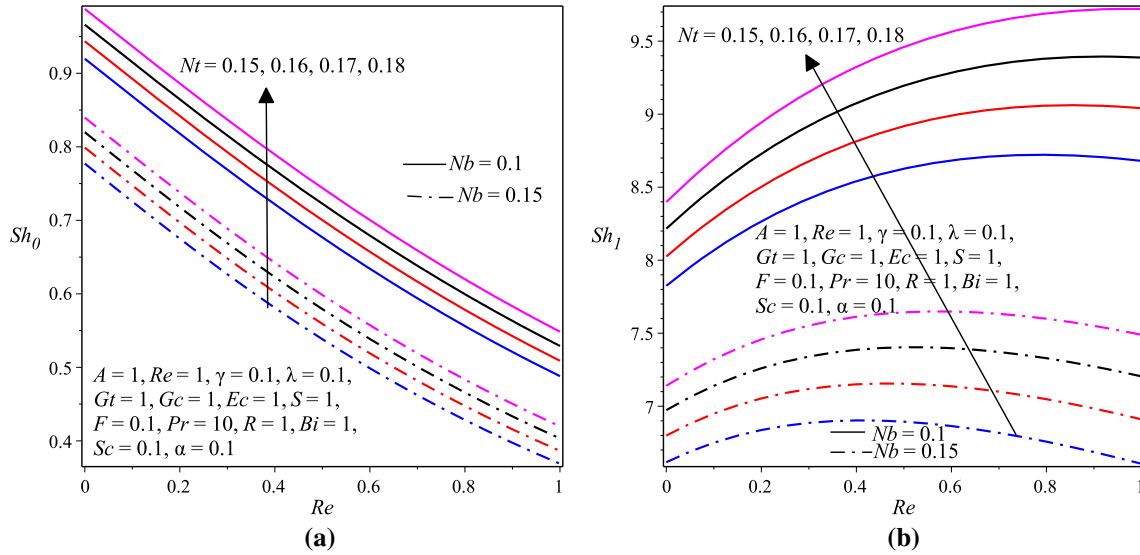


Fig. 24 a Sh at $\eta = 0$ and b Sh at $\eta = 1$ with varying Nt, Nb and Re

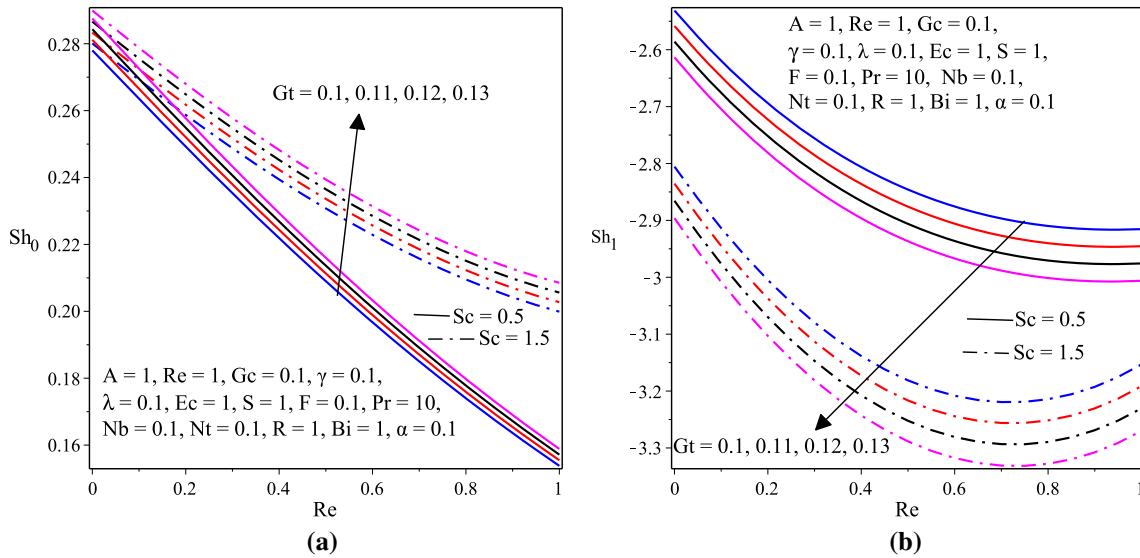


Fig. 25 a Sh at $\eta = 0$ and b Sh at $\eta = 1$ with varying Sc, Gt and Re

be seen that the wall heat transfer rate, the Nusselt number Nu at both cold and hot walls show an increasing behavior with increasing the values of the variable viscosity parameter γ , the Brownian motion parameter Nb and the porous medium shape parameter S for varying scaled values of the suction/injection Reynolds number Re . Nevertheless, the variable thermal conductivity parameter λ , the thermophoresis parameter Nt , the radiation parameter R and the Eckert number Ec show a decreasing effect on Nu at both walls of the microchannel. As presented in Figs. 20a, b, 21a, b, the Nusselt number Nu increases with increasing values of the Schmidt number Sc , the Grashof number Gt and the Biot number Bi , respectively, at the cold wall of the microchannel $\eta = 0$, but the reverse trend is observed at the hot wall $\eta = 1$ of the microchannel.

5.3.3 The wall mass transfer rate: Sherwood number

The effects of embedded governing flow parameters on the wall mass transfer rate at the cold wall $\eta = 0$ and at the hot wall $\eta = 1$ are displayed in Figs. 22a, 23, 24, 25 and 26b. As a result, these graphs indicate that the wall mass transfer rate, the Sherwood number Sh at both cold and hot walls show an increasing behavior with increasing values of the porous medium shape parameter S , the variable viscosity parameter

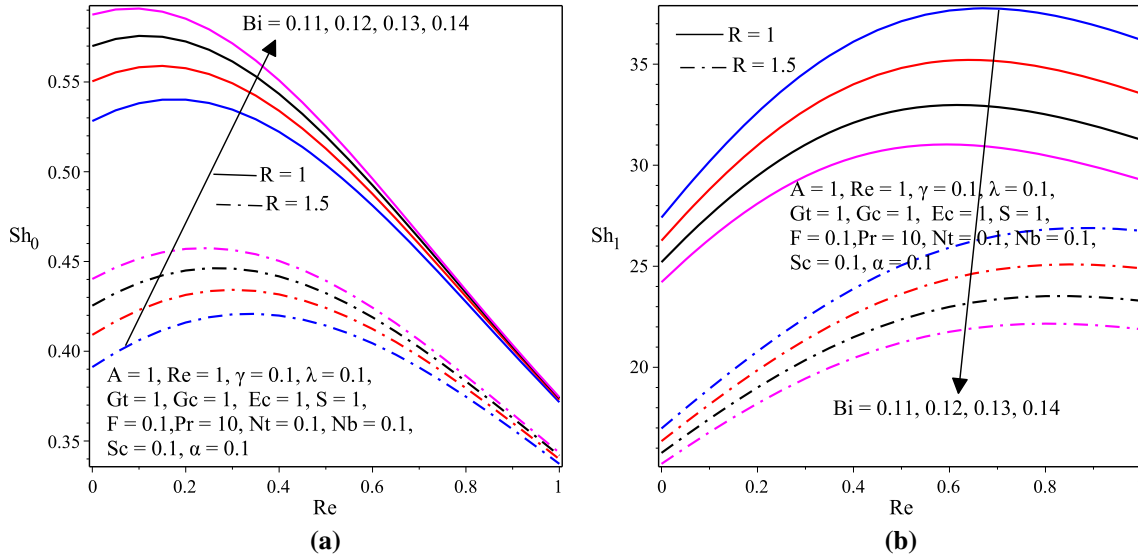


Fig. 26 **a** Sh at $\eta = 0$ and **b** Sh at $\eta = 1$ with varying Bi , R and Re

γ and the thermophoresis parameter Nt for varying scaled values of the suction/injection Reynolds number Re . However, the Eckert number Ec , the variable thermal conductivity parameter λ , the Brownian motion parameter Nb and the radiation parameter R show a decreasing effect on Sh at both walls of the microchannel. Figures 25a, b, 26a, b present that the Sherwood number Sh rises with rising values of the Schmidt number Sc , the Grashof number Gt and the Biot number Bi , respectively, at the cold wall $\eta = 0$, but the opposite is observed at the hot wall $\eta = 1$ of the microchannel.

6 Conclusion

Radiating and reacting nanofluids flow in microchannels with non-uniform permeable walls temperature and filled with porous media plays an important role in the modern industrial and engineering applications. The applications include electronics cooling, engine cooling, cooling towers, aerospace technology, cancer therapy, drug delivery applications, solar cell panels, geothermal extraction, crude oil extraction, underground water movement, chemical industry, drying and dehydration operations, oxidation of solid materials, manufacturing of ceramics and glassware, nuclear power, missiles, satellites and so on.

Therefore, this paper presented the investigation of hydrodynamical characteristics and heat transfer properties of radiating and reacting nanofluid with variable transport properties in a microchannel filed with a saturated porous medium by taking into account the convective boundary conditions. The flow medium was considered to be porous with the combination of Darcy–Forchheimer medium. The Buongiorno’s nanofluid flow model was also used to study the effects of the Brownian motion and the thermophoresis. The governing highly nonlinear partial differential equations were solved numerically by utilizing the semi-discretization finite difference method. Graphs were used to analyze the effects of the emerging thermophysical parameters on the nanofluid velocity, temperature and nanoparticle concentration as well as on the coefficient of skin friction, heat transfer and mass transfer rates. Consequently, the following are important findings of the present study.

- Both the velocity and temperature profiles of the nanofluid show an increasing behavior with increasing values of variable viscosity parameter γ , Eckert number Ec , thermal Grashof number Gt , solutal Grashof number Gc , Prandtl number Pr and chemical reaction parameter α .
- The concentration profile indicates an increasing trend with increasing values of variable thermal conductivity parameter λ , porous medium shape parameter S , Forchheimer number F , Schmidt number Sc , Brownian motion parameter Nb , radiation parameter R and Biot number Bi .
- The skin friction coefficient C_f is large for higher values of suction/injection Reynolds number Re , porous medium shape parameter S , thermal Grashof number Gt , Schmidt number Sc and Brownian motion parameter Nb on both sides of the microchannel walls.

- The heat transfer and mass transfer rates on both sides of the microchannel walls indicate an increasing behavior for increasing values of suction/injection Reynolds number Re , porous medium shape parameter S , variable viscosity parameter γ but a decreasing behavior for increasing values of Eckert number Ec , variable thermal conductivity parameter λ and radiation parameter R .
- Grashof number Gr , Schmidt number Sc and Biot number Bi indicate an increasing effect on both the heat transfer and mass transfer rates at the cold wall of the microchannel.
- The Brownian motion parameter Nb and the thermophoresis parameter Nt show an opposite effect on the heat transfer and mass transfer rates on both sides of the microchannel walls.

Acknowledgements The authors are very much thankful for the constructive comments and suggestions of the editor as well as the anonymous reviewers, which led to improvement of the paper. The corresponding author is very grateful to the financial support of Adama Science and Technology University (Grant No. ASTU/SP-R/073/20).

Declarations

Conflict of interest The authors declare that they have no known competing interests that could have appeared to influence the work reported in this paper.

References

1. Rai, S.K., Sharma, R., Saifi, M., Tyagi, R., Singh, D., Gupta, H.: Review of recent applications of microchannel in MEMS devices. *Int. J. Appl. Eng. Res.* **13**(9), 64–69 (2018)
2. Jahangiri, M., Farsani, R.Y., Shamsabadi, A.A.: Numerical investigation of the water/alumina nanofluid within a microchannel with baffles. *J. Mech. Eng. Tech.* **10**(2) (2018)
3. Saleel, C.A., Algahtani, A., Badruddin, I.A., Khan, T.M.Y., Kamangar, S., Abdelmohimen, M.A.H.: Pressure-driven electro-osmotic flow and mass transport in constricted mixing microchannels. *J. Appl. Fluid Mech.* **13**(2) 429–441 (2019). <https://doi.org/10.29252/jafm.13.02.30146>
4. Reddy, K.V., Makinde, O.D., Reddy, M.G.: Thermal analysis of MHD electro-osmotic peristaltic pumping of Casson fluid through a rotating asymmetric microchannel. *Indian J. Phys.* **92**(11), 1439–1448 (2018). <https://doi.org/10.1007/s12648-018-1209-1>
5. Kmiotek, M., Kucab-Pietal, A.: Influence of slim obstacle geometry on the flow and heat transfer in microchannels. *Bull. Polish Acad. Technol. Sci.* **66**(2) (2018). <https://doi.org/10.24425/119064>
6. Ahadi, A., Antoun, S., Saghir, M.Z., Swift, J.: Computational fluid dynamic evaluation of heat transfer enhancement in microchannel solar collectors sustained by alumina nanofluid. *Energy Storage*, **1**(e37) (2019). <https://doi.org/10.1002/est.37>
7. Venkateswarlu, M., Prameela, M., Makinde, O.D.: Influence of heat generation and viscous dissipation on hydromagnetic fully developed natural convection flow in a vertical microchannel. *J. Nanofluids* **8**(7), 1506–1516 (2019). <https://doi.org/10.1166/jon.2019.1692>
8. Moon, J., Pacheco, J.R., Pacheco-Vega, A.: Heat transfer enhancement in wavy microchannels: effect of block material. In: Proceedings of the 4th World Congress on Momentum, Heat and Mass Transfer (MHMT'19), Rome Italy, *ENFHT* **120** 1–11 (2019). <https://doi.org/10.11159/enfht19.120>
9. Dewan, A., Srivastava, P.: A review of heat transfer enhancement through flow disruption in a microchannel. *J. Therm. Sci.* **24**(3), 203–214 (2015). <https://doi.org/10.1007/s11630-015-0775-1>
10. Choi, S.U.S.: Enhancing thermal conductivity of fluids with nanoparticles. *ASME Fluids Eng. Div.* **231**, 99–105 (1995)
11. Jedi, A., Shamsudeen, A., Razali, N., Othman, H., Zainuri, N.A., Zulkarnain, N., Abu Bakar, N.A., Pati, K.D., Thanoon, T.Y.: Statistical modeling for nanofluid flow: a stretching sheet with thermophysical property data. *Colloids Interfaces*, **4**(3) (2020). <https://doi.org/10.3390/colloids4010003>
12. Subramanian, K.R.V., Rao, T.N., Balakrishnan, A.: *Nanofluids and Their Engineering Applications*. Taylor & Francis Group, CRC Press (2020)
13. Xu, H., Huang, H., Xu, X.H., Sun, Q.: Modeling heat transfer of nanofluid flow in microchannels with electrokinetic and slippery effects using Buongiorno's model. *Int. J. Numer. Methods for Heat Fluid Flow.* (2019). <https://doi.org/10.1108/HFF-09-2018-0506>
14. Patel, A.K., Bhuvad, S., Rajput, S.P.S.: Effects of nanofluid flow in microchannel heat sink for forced convection cooling of electronics device: a numerical simulation. *Int. J. Innovative Tech. Exploring Eng.*, **9**(2) 5230–5243 (2019). <https://doi.org/10.35940/ijtee.A4122.129219>
15. Niazi, M.D.K., Xu, H.: Modelling two-layer nanofluid flow in a microchannel with electro-osmotic effects by means of the Buongiorno's model. *Appl. Math. Mech.* **41**(1) 83–104 (2020). <https://doi.org/10.1007/s10483-020-2558-7>
16. Shahrestani, M.I., Maleki, A., Shadloo, M.S., Tlili, I.: Numerical investigation of forced convective heat transfer and performance evaluation criterion of Al_2O_3 /water nanofluid flow inside an axisymmetric microchannel. *Symmetry* **12**(120), 1–17 (2020). <https://doi.org/10.3390/sym12010120>
17. Muhammad, H., Muhammad, U., Rizwan, U.H., Zhenfu, T.: A Galerkin approach to analyze MHD flow of nanofluid along converging/diverging channels. *Arch. Appl. Mech.* **91**, 1907–1924 (2021). <https://doi.org/10.1007/s00419-020-01861-6>
18. Feroz, A.S., Rizwan, U.H., Muhammad, H.: Brownian motion and thermophoretic effects on non-Newtonian nanofluid flow via Crank–Nicolson scheme. *Arch. App. Mech.* **91**, 3303–3313 (2021). <https://doi.org/10.1007/s00419-021-01966-6>

19. Mahmoudi, Y., Hooman, K., Vafai, K.: *Convective Heat Transfer in Porous Media*. Taylor & Francis Group. CRC Press (2020)
20. Al-Rashed, A.A.A.A., Sheikhzadeh, G.A., Aghaei, A., Monfared, F., Shahsavari, A., Afrand, M.: Effect of a porous medium on flow and mixed convection heat transfer of nanofluids with variable properties in a trapezoidal enclosure. *J. Therm. Anal. Calorimetry* (2019). <https://doi.org/10.1007/s10973-019-08404-4>
21. Muthamilselvan, M., Ureshkumar, S.S.: A tilted Lorentz force effect on porous media filled with nanofluid. *J. Theor. Appl. Mech. Sofia* **48**(2), 50–71 (2018). <https://doi.org/10.2478/jtam-2018-0010>
22. Shashikumar, N.S., Prasannakumara, B.C., Gireesha, B.J., Makinde, O.D.: Thermodynamics analysis of mhd casson fluid slip flow in a porous microchannel with thermal radiation. In: *Diffusion Foundations, Switzerland*. Trans Tech Publications **16**, 120–139 (2018). <https://doi.org/10.4028/www.scientific.net/DF.16.120>
23. Gireesha, B.J., Srinivasa, C.T., Shashikumar, N.S., Macha, M., Singh, J.K., Mahanthesh, B.: Entropy generation and heat transport analysis of Casson fluid flow with viscous and Joule heating in an inclined porous micro-channel. *Proc. I Mech. Eng. Part E: J. Process Mech. Eng.* **0**(0) 1–12 (2019). <https://doi.org/10.1177/0954408919849987>
24. Aina, B., Malgwi, P.B.: MHD convection fluid and heat transfer in an inclined micro-porous-channel. *Nonlinear Eng.* **8**, 755–763 (2019). <https://doi.org/10.1515/nleng-2018-0081>
25. Muhammad, M., B., Chaudry, M.K., Lehlohonolo, P.: Heat transfer effects on electro-magnetohydrodynamic Carreau fluid flow between two micro-parallel plates with Darcy-Brinkman-Forchheimer medium. *Arch. Appl. Mech.* **91** 1683–1695 (2021). <https://doi.org/10.1007/s00419-020-01847-4>
26. Suresh Babu, R., Kumar, R.B., Makinde, O.D.: (2018). Chemical reaction and thermal radiation effects on MHD mixed convection over a vertical plate with variable fluid properties. *Defect Diffusion Forum*, **387** 332–342 (2018)
27. Nayak, M.K., Sachin, S., Makinde, O.D.: Chemically reacting and radiating nanofluid flow past an exponentially stretching sheet in a porous medium. *Indian J. Pure Appl. Phys.* **56**, 773–786 (2018)
28. Sharma, R.P., Makinde, O.D., Animasaun, I.L.: Buoyancy effects on MHD Unsteady convection of a radiating chemically reacting fluid past a moving porous vertical plate in a binary mixture. *Defect Diffusion Forum* **387**, 308–318 (2018). <https://doi.org/10.4028/www.scientific.net/DDF.387.308>
29. Makinde, O.D., Mbood, F., Ibrahim, M.S.: Chemically reacting on MHD boundary-layer flow of nanofluids over a non-linear stretching sheet with heat source/sink and thermal radiation. *Therm. Sci.* **22**, 495–506 (2018). <https://doi.org/10.2298/TSCI151003284M>
30. Reddy, B.P.: Radiation and chemical reaction effects on unsteady MHD free convection parabolic flow past an infinite isothermal vertical plate with viscous dissipation. *Int. J. Appl. Mech. Eng.* **24**(2), 343–358 (2019). <https://doi.org/10.2478/ijame-2019-0022>
31. Matao, P.M., Reddy, B.P., Sunzu, J.M., Makinde, O.D.: Finite element numerical investigation into unsteady MHD radiating and reacting mixed convection past an impulsively started oscillating plate. *Int. J. Eng. Sci. Tech.* **12**(1), 38–53 (2020). <https://doi.org/10.4314/ijest.v12i1.4>
32. Zigta, B.: Mixed convection on MHD flow with thermal radiation, chemical reaction and viscous dissipation embedded in a porous medium. *Int. J. Appl. Mech. Eng.* **25**(1), 219–235 (2020). <https://doi.org/10.2478/ijame-2020-0014>
33. Hamid, M., Usman, M., Khan, Z. H., Haq, R. U., Wang, W.: Numerical study of unsteady MHD flow of Williamson nanofluid in a permeable channel with heat source/sink and thermal radiation. *Eur. Phys. J. Plus* **133**(527), 1–12 (2018). <https://doi.org/10.1140/epjp/i2018-12322-5>
34. Buongiorno, J.: Convective transport in nanofluids. *J. Heat Transf.* **128**, 240–250 (2006)
35. Rundora, L., Makinde, O.D.: Buoyancy effects on unsteady reactive variable properties fluid flow in a channel filled with a porous medium. *J. Porous Media* **21**(8), 721–737 (2018)
36. Hindebu, B., Makinde, O. D., Guta, L.: Unsteady mixed convection flow of nanofluid in a micro-channel filled with a porous medium. *Indian J. Phys.* 1–18 (2021). <https://doi.org/10.1007/s12648-021-02116-y>
37. Hamid, M., Zubair, T., Usman, M., Haq, R.U.: Numerical investigation of fractional-order unsteady natural convective radiating flow of nanofluid in a vertical channel. *AIMS Math.* **4**(5), 1416–1429 (2019). <https://doi.org/10.3934/math.2019.5.1416>
38. Makinde, O.D., Khan, Z.H., Ahmad, R., Haq, R.U., Khan, W.A.: Unsteady MHD flow in a porous channel with thermal radiation and heat source/sink. *Int. J. Appl. Comput. Math.* **559**, 1–21 (2019). <https://doi.org/10.1007/s40819-019-0644-9>
39. Monaledi, R.L., Makinde, O.D.: Entropy analysis of a radiating variable viscosity EG/Ag nanofluid flow in microchannels with buoyancy force and convective cooling. *Defect Diffusion Forum* **387**, 273–285 (2018). <https://doi.org/10.4028/www.scientific.net/DDF.387.273>
40. Bhandari, A.: Radiation and chemical reaction effects on nanofluid flow over a stretching sheet. *Fluid Dyn. Mater. Process. FDMP* **155**, 557–582 (2019)
41. Venkateswarlu, M., Makinde, O.D., Lakshmi, D.V.: Influence of thermal radiation and heat generation on steady hydromagnetic flow in a vertical micro-porous-channel in presence of suction/injection. *J. Nanofluids* **8**(5), 1010–1019 (2019)
42. Rundora, L., Makinde, O.D.: Unsteady MHD flow of non-Newtonian fluid in a channel filled with a saturated porous medium with asymmetric navier slip and convective heating. *Appl. Math. Inf. Sci.* **12**(3) 483–493 (2018). <https://doi.org/10.18576/amis/120302>
43. Sujatha, T., Reddy, K.J., Kumar, J.G.: Chemical reaction effect on nonlinear radiative MHD nanofluid flow over cone and wedge. *Defect Diffusion Forum* **393**, 83–102 (2019)
44. Ramzan, M., Rafiq, A., Chung, J.D., Kadry, S., Chu, Y.M.: Nanofluid flow with autocatalytic chemical reaction over a curved surface with nonlinear thermal radiation and slip condition. *Sci. Rep.* **10**, 1–13 (2020). <https://doi.org/10.1038/s41598-020-73142-9>